Influence of Humidity, Temperature, and the Addition of Activated Carbon on the Preparation of Cellulose Acetate Membranes and Their Ability to Remove Arsenic from Water

Luisa Piroshka Terrazas-Bandala,[1,2] Guillermo Gonzalez-Sanchez,[1] Ricard Garcia-Valls,[3] Tania Gumi,[3] Isabelle Beurroies,[4] Renaud Denoyel,[4] Carles Torras,[5] Lourdes Ballinas-Casarrubias[2]

[1]Department of Renewable Energies and Environmental Protection, Centro de Investigación en Materiales Avanzados (CIMAV S.C.), Chihuahua, Chih, México
[2]Graduate Department, Facultad de Ciencias Químicas, Universidad Autónoma de Chihuahua (UACH), Chihuahua, Chih, México
[3]Department of Chemical Engineering, ETSEQ—Universitat Rovira i Virgili, Tarragona, Spain
[4]Laboratoire Madirel, CNRS-Université de Provence, Marseille, France
[5]Catalonia Institute for Energy Research, IREC, Marcel·lí Domingo 2, 43007 Tarragona, Spain
Correspondence to: L. Ballinas-Casarrubias (E-mail: mballinas@uach.mx)

ABSTRACT: Several composite membranes have been prepared from cellulose triacetate (CTA) and activated carbon (AC) by solvent casting, varying temperature from 35 to 55°C and relative humidity (RH): 10–70%. Some conditions promoted AC particle agglomeration which is evidenced by SEM and IFME® program. In those membranes, where homogeneity is attained, a deep characterization has been carried out by DMA, MDSC, thermoporometry, solute transport, and AFM. When AC is added in films, T_g is lowered and the fraction of pores with bigger size is augmented. Molecular weight cut off calculated by solute transport, increases from 801.15 to 1194.29 kDa using 1% AC at RH 70% and T 35°C. Water flux is of 5.23 $Lm^{-2} h^{-1} bar^{-1}$. Arsenic removal has been performed, achieving a 45% tested from a 500 ppb arsenic solution, where several factors such as electrical rejection, adsorption and exclusion, could contribute to the total membrane nanofiltration process. © 2013 Wiley Periodicals, Inc. J. Appl. Polym. Sci. **2014**, *131*, 40134.

INTRODUCTION

Membrane technologies are considered an advanced method for the purification of water. Rejection is determined by the properties of the membrane (pore size distribution, adsorption characteristics, and charge) and by the operating conditions (e.g., pressure, pH and ionic strength of the solution). Nanofiltration and reverse osmosis are useful for separation of heavy metals, metalloids, and salts, and especially for highly mineralized waters, with elements such as arsenic.[1] Arsenic is a common naturally occurring metalloid. Geochemical contamination through mineral leaching is the primary contributor of dissolved arsenic in ground water around the world. In 1994 the National Water Commission in Mexico made a hydrologic study and found arsenic concentrations from 0.05 to 0.5 mg L^{-1} in well water of the Northwest region.[2] To decrease arsenic in water for human consumption, the Mexican government has set around 200 reverse osmosis membrane plants to purify water. Nevertheless, membrane replacement has a strong dependence upon the usage of imported materials, raising the cost for its operation. In an intention to substitute general used membrane materials with low cost ones, several attempts have been done to obtain films made of cellulose and organic fillers.[3–6] Particularly, it has been reported the preparation of nanocomposite membranes by water vapor induced phase separation (VIPS) of cellulose triacetate (CTA) and activated carbon particles (AC) for use in water purification treatment; specifically for the removal of inorganic arsenic form drinking water.[7] In this work a deeper insight into the modification of CTA membranes by activated carbon addition is pretended. In a previous study using polysulfone and AC, composite membranes by immersion-precipitation were obtained.[8] AC was evidenced as a microparticle after its suspension in THF, during membrane preparation. This reduction process was also evaluated into CTA membranes obtained by casting. AC microparticles are incorporated into the polymeric matrix, and an improvement on Young modulus was obtained for the best dispersion conditions.[5] Those findings lead to several studies on CTA–AC composites that suggest the AC is

not only affecting the mechanical properties. In addition to this improvement, the AC is still acting as an adsorbent, i.e., it does not lose its adsorption capacity in metal removal, and moreover the total capacity of the composite is better than the one is regarded with the AC in a batch test. These findings have already reported for uranium removal in water.[9] In this context, the present study contributes also to understand the influence of synthesis parameters on properties of CTA-AC membranes used in this case, for arsenic removal.

The combination of organic polymers with organic particles, for the preparation of membranes, has been widely studied.[10–12] In most cases, when good dispersion of the particles in the polymer matrix was achieved, the selectivity and flux properties were enhanced. To understand the reasons for this change in selectivity properties, several techniques have been used, including measurements of mechanical properties, determination of the crystal/amorphous phase ratio, surface roughness, pore size and pore size distribution. The best interpretations are generally obtained when using various techniques simultaneously and by comparing their results.

In this work, a preselection of membrane materials was performed by the calculus made using IFME® of several scanning electron micrographies. Particle aggregation was evidenced for some of the casting conditions. Dynamical mechanical analysis and modulated differential scanning calorimetry were performed to membranes where nonparticle aggregates were found. In membrane composites, homogeneity is a special challenge when solid fillers are used.[10]

So in order to complete the structural characterization and to get a deeper understanding of the behavior of these composite membranes, it is necessary to measure their pore size distribution. It is an instrumental challenge to distinguish differences at the nano-scale in dense homogenous materials such as the ones obtained with cellulose triacetate by evaporation-precipitation. There are several well-established techniques for these measurements, among them are the bubble point technique, mercury porometry, microscopic techniques, solute transport, permporometry and thermoporometry.[13]

Thermoporometry is a method for measuring pore size distribution, based on the depression of melting temperature of materials constrained within small pores.[14,15] The merits of this method are that pore structures can be measured in the wet environments in which in fact are actually used. For instance, the structure change during sample preparation and observation can be minimized.[16] During the last two decades, thermoporometry has been used for various porous solids having disordered structures,[17,18] and different kinds of porous membranes.[19–21]

Since the invention of the atomic force microscope (AFM), it has been applied extensively for studying micro, ultra and nano-filtration membranes.[22,23] There are several tools available to determine many morphological, structural, and textural parameters of membranes, including surface roughness, symmetry, grain size, and nodule size. Pore size and pore size distribution are often determined by visual inspection of the different line profiles of cross sections, which have been chosen randomly on a given image.

There are numerous studies in which, in an attempt to obtain information about the pore size distribution of the membrane, the relationship between the solute separation and the size of the solute has been examined. Studies directed by Khulbe and Matsuura to characterize ultrafiltration membranes have used polyethylene glycol of different weights, to calculate molecular weight cut-off (MWCO), mean pore size, and surface porosity. Their results were in good agreement with those obtained by AFM image analysis.[22–24]

In the present study, these three characterization techniques: thermoporometry, the method based on solute transport and AFM, were used to measure the pore size distribution and molecular weight cut off of composite membranes of triacetate cellulose and activated carbon particles prepared by water vapor induced phase separation. For all the techniques tested for porosity measurement, the same tendencies are evidenced. They reveal that carbon loading increased the fraction of pores with bigger size, increasing thus MWCO for the analyzed membranes. Furthermore, composites obtained at 35°C and 1% CL presented the best particle dispersion and higher Young module (1.3 GPa). Using this material in a nanofiltration process, a 45% removal from a 500 ppb arsenic solution was attained.

THEORY

Thermoporometry

The freezing thermograms could be monitored in a differential scanning calorimeter (DSC). The pore radius (R_p), and differential pore volume (dV/dR_p) were calculated from both, the characteristic undercooling (ΔT, °C) and heat flow (dq/dt), with the following equations[14]:

$$Rp = 0.57 - \frac{64.67}{\Delta T} \text{ (in nm)} \tag{1}$$

$$\frac{dV}{dRp} = \frac{k(\Delta T^2)(dq/dt)}{\Delta H_a(T)} \tag{2}$$

where k is a "calibration constant" in accordance with the instrument sensitivity, sample mass and heating rate, and $\Delta H_a(T)$ is the apparent transition energy (J g^{-1}).

$$\Delta H_a(T) = 0.0556(\Delta T)^2 + 7.43\Delta T + \Delta H_f \tag{3}$$

ΔH_f is the heat of fusion for the penetrant liquid under normal conditions (332 J g^{-1} for water).

Solute Separation

The solute separation (f), obtained from membrane filtration experiments, using polyethylene glycol (PEG) and Polyethylene oxide (PEO) of different molecular weights, is defined as:

$$f = \left(1 - \frac{C_p}{C_f}\right) \times 100 \tag{4}$$

where C_p and C_f are the solute concentration in permeate and in the bulk of the feed solution respectively. The data were transferred to a log-normal probability plot of solute separation

(*f*) versus the solute diameter (sd). The latest was obtained from the Einstein–Stokes radius (ESr, [nm]) which corresponds to the molecular weight (*M*, [kDa]) of the solute with the following equations[25]:

$$ESr = 16.73 \times 10^{-10} M^{0.557} \tag{5}$$

for PEG and

$$ESr = 10.44 \times 10^{-10} M^{0.587} \tag{6}$$

for PEO, respectively.

From this log-normal probability plot, MWCO was obtained from the solute diameter at *f* = 90%. The mean pore size (μ_p) was calculated as the solute diameter that corresponds to *f* = 50%, and the geometric standard deviation, (σ_p) was obtained from the ratio of the solute diameter at *f* = 84.13 and at 50%.

By ignoring the dependence of the solute separation on the steric and hydrodynamic interaction between solute and pore sizes,[24] the mean pore size (μ_p) and the geometric standard deviation (σ_p) of the membrane were considered to be the same as of the solute mean size and the solute geometric standard deviation respectively. From the values of μ_p and σ_p, the pore size distribution of a filtration membrane can be expressed by the following probability density function[26]:

$$\frac{df(d_p)}{dd_p} = \frac{1}{d_p \ln \sigma_p \sqrt{2\pi}} \exp\left[-\frac{\left(\ln d_p - \ln \mu_p\right)^2}{2\left(\ln \sigma_p\right)^2} \right] \tag{7}$$

where d_p is the pore size in nm.

Surface porosity *Sp*, defined as the ratio between the areas of pores to the total membrane surface area was calculated using the equation[24]:

$$Sp = \left(\frac{N\pi}{4} \sum_{d\,\min}^{d\,\max} f_i d_i^2 \right) \times 100 \tag{8}$$

where *N* is the total number of pores per unit area (pore density as pores/μ^2) and f_i the fraction of the number of pores with diameter d_i. *N* was determined using the following equation:

$$N = \frac{128 \eta \delta J}{\pi \Delta P \sum_{d\,\min}^{d\,\max} f_i d_i^4} \times 100 \tag{9}$$

where δ is the length of the pores and is considered to be equal to the membrane thickness; η is the solvent viscosity (Pa s^{-1}); ΔP the trans membrane pressure in Pa and *J* the solvent flux in μ^3/μ^2s.

EXPERIMENTAL

Membrane Samples
The membranes were prepared in a controlled humidity chamber (Shell Lab) at different sets of temperature and relative humidity (35, 45, and 55°C; 10, 40, 70%, respectively). The cellulose triacetate (Sigma–Aldrich) was dissolved and activated carbon (LQ-1000, Carbochem) nanoparticles were suspended into methylene chloride separately (3.3% w/v CTA; 0–3% w/v AC, respectively) and stirred at a controlled temperature (25°C) for 24 h.[7] The solutions were mixed to obtain the casting one. The casting solutions were uniformly spread over a glass dish of 14 × 19 cm^2. The precipitation was performed in a controlled chamber for 2 h. The samples were removed with distilled water and were stored in dry conditions at room temperature. For each condition three replicates were made.

Scanning Electron Microscopy and IFME Calculations
Membranes produced were put in contact with liquid nitrogen, fractured and then treated further in a covering system (Denton Desk-II Gatan) with gold. Afterwards, they were characterized by scanning electron microscopy (SEM JEOL JSM5800-LV). SEM photomicrographs were taken at 15 kV, in top and edge views. The structures were analyzed at a magnification of 300×. IFME is copyrighted software created specifically to treat and analyze membrane images obtained with the SEM,[27] which accomplishes with the desired functions for pore analysis, and structural dimensions of the material.

Dynamic Mechanical Analysis
Stress-strain tests for films were made in a dynamic mechanical analyzer (DMA) RSA III from TA Instruments. A fixture was used for evaluating tensile properties of thin films. Averages of the elastic modulus and ultimate stress and strain were obtained using three repetitions (*n* = 3) for each one of the membranes tested. The temperature was kept constant at 25 or 100°C and the extension rate employed was 0.005 mm s^{-1}. Sample dimensions were 8 mm in length and 0.384 mm^2 in transversal areas. Same instrument was used to perform temperature scan tests. The storage modulus (*E*′), the loss modulus (*E*″), and the tangent loss (tan δ) were obtained at 6.28 rad s^{-1} (Hz), between 90°C and 260°C, with a temperature change rate of 5°C min^{-1}. The initial deformation was set at 0.1%. The initial static strain was of 38 g with a tensor distance of 8 mm. All data were analyzed with TA Orchestrator V.7.0.8.23 TA Instruments® software.

Modulated Scanning Calorimetry
The MDSC measurements were carried out using a 2920 TA Instruments device in the temperature range from 28 to 265°C with a heating rate of 5°C min^{-1} and a modulated shift of 1°C/80 s. The sample weights were ~5 mg. All samples were sealed in aluminum pans and the measurements were performed under air atmosphere.

Thermoporometry Measurements
The DSC measurements were made using a differential scanning calorimeter (DSC 92-Setaram), with a controlled cooling accessory to lower the block temperature to −80°C. Wet film samples (5–10 mg) were sealed in tared aluminum DSC pans. The temperature was dropped rapidly to −80°C, and held for several minutes to freeze the water, as indicated by an exothermic peak. The samples were then heated (at a rate of 5°C min^{-1}) to −0.15°C and held there for 1200 s (enough time for the water in the pores to melt), the temperature was then dropped at the

same rate to $-80°C$. The freezing of the water in the pores was observed as an exothermic peak below $0°C$. The final step was the melting of all the water at a controlled rate. For the sake of comparison, some measurements were also made with different heating rates and extra amount of water. The instrumental baseline was checked using two similar empty pans; temperature and heat flow calibration were checked with pure water.

After completing the DSC measurements, the sample pans were reweighed (to check that water had not evaporated during the experiment). The sample pans were punctured and then dried to constant weight of water, which had been contained in the sample.

Solute Transport Experiments

The filtration experiments were performed using a SEPA GE-Osmonics cell, which was operated at a constant transmembrane pressure of 1.4 MPa and a constant fluid recirculating temperature between 20 and $25°C$. The membrane area was of 144 cm^2. The membranes were characterized in the module after pretreatment with pure water for 8 h. The pure water permeation (PWP) flux was measured for each membrane by circulating distilled water through the membrane system, before starting the corresponding solute transport experiment. Polyethylene glycol (PEG) molecular weight of 8,000, 20,000, and 35,000 Da, and polyethylene oxide (PEO) molecular weight 100 and 200 Da, were used as the solutes in the feed solutions for the filtration experiments. The initial feed concentration was 200 ppm. PEG-PEO separation experiments were conducted starting from the lower molecular weight solute. The system was thoroughly flushed with distilled water between runs made with PEG-PEO solutes of different molecular weights. The PEG solutions were analyzed using spectrophotometry, and the following method (3.6.1).

PEG and PEO Determination by Spectrophotometry. Four milliliters of sample solution were added to 1 mL 5% (w/v) $BaCl_2$ (Baker) in 1 N HCl. To this mixture, a 1 mL of solution prepared by dissolving 1.27 g of I_2 in 100 mL 2% KI (w/v) solution was added, which is further diluted 10 times. Reaction occurred for 15 min at room temperature, and absorption was measured using a spectrophotometer (Perkin Elmer, Lambda) at 535 nm against a reagent blank.

Pore Distribution by AFM Images

The AFM characterization was performed using a Nanoscope IV AFM from Digital Instruments. The samples were mounted on a stainless steel disk with a sticky tap. Scanning rates in the range of 2–3 Hz were used. The images were recorded in the tapping mode, using etched silicon probes (Digital Instruments). The parameters, specially the set point and the drive amplitude, were adjusted to obtain the best image resolution. For every sample, images were collected at different locations in order to obtain reproducible and reliable images.

Arsenic Removal

Synthetic aqueous solutions of different arsenic concentrations were made (100, 300, and 500 ppb) from an arsenic (V) standard (1000 ppm Aldrich in HNO_3 2%). Pentavalent arsenic could be present in solution as H_3AsO_4, $H_2AsO_4^-$ $HAsO_4^{2-}$ and AsO_4^{3-}. These species are pH- and redox dependent. For the pH of the experiments, adjusted at pH $= 6$, calculated molar concentration for the more concentrated solution (500 ppb) using the Medusa software[28] are: $H_3AsO_4 = 1 \times 10^{-6.1}$, $H_2AsO_4^- = 1 \times 10^{-2.3}$ $HAsO_4^{2-} = 1 \times 10^{-3.03}$ and $AsO_4^{3-} = 1 \times 10^{-8.6}$ at a potential $E = 500$ mV. This software considers the more actualized data for the equilibrium constants reported.[28] Thus, anionic species are the ones that prevail in the conditions fixed experimentally using the arsenic synthetic solutions. Conductivity measurements were done using a conductivity meter (Thermo Fisher Scientific). A continuous flux cell (Sepa GE-Osmonics) was operated as described in Solute Transport Experiments section. The membrane area was of 144 cm^2. The operation time was of 5 h for each membrane after reaching the stationary state. Hydride generation atomic absorption spectrometry was used for arsenic analysis (Perkin Elmer 3100). The equipment was set as follows: Wave length: 193.7 nm; slit 0.7, argon flux of 50 mL min^{-1}. Arsenite was analyzed according to measurements performed by an auxiliary technique, specified elsewhere (automated hydride generation cryotrapping-atomic absorption spectrometry).[7]

RESULTS AND DISCUSSION

SEM Analysis and IFME Calculation

Several scanning electron micrographs were obtained for the membranes prepared. In the case where pure CTA was used for membrane synthesis, a dense film was evidenced by SEM. In some conditions, when carbon was used as filler, some aggregates appear due to agglomeration of the particles. An example of the aggregates obtained in some of the casting conditions is shown in Figure 1, and their corresponding analysis by IFME is detailed in Table I.

The calculations performed by IFME for the mean aggregate diameters, reveal differences in particle agglomeration during casting conditions. Throughout the analysis, we did not consider as aggregate particles the ones just supported and not confined by the structure (see at $55°C$, 40% RH and 1% CL; and the ones at $35°C$ for 3% CL); even though these films are not uniform.

In this analysis, the morphology of membrane could change from a dense homogeneous structure to a heterogeneous one, with visible superficial cumulus. The physicochemical phenomenon which dictates membrane morphology is influenced by thermodynamic and kinetic constraints, regarding principally to the solvent evaporation process. In this sense, the two principal variables affecting the synthesis were relative humidity (RH) and temperature. The relative humidity affects in the following manner:

1. Water vapor acts as a nonsolvent, so depending on its concentration in the casting atmosphere, the efficacy of the precipitation varies. At high RH, water penetrates more efficiently into the polymer. This condition assures adequate AC particle dispersion. In membranes obtained at constant temperature, the more homogeneous films are obtained when elevated humidity is used (Table I, see 1% CL).
2. Solvent (CH_2Cl_2) diffusion decreases at high water vapor concentration. This condition is known as VIPS process.[29] If the diffusion of the solvent is slow, denser membranes will
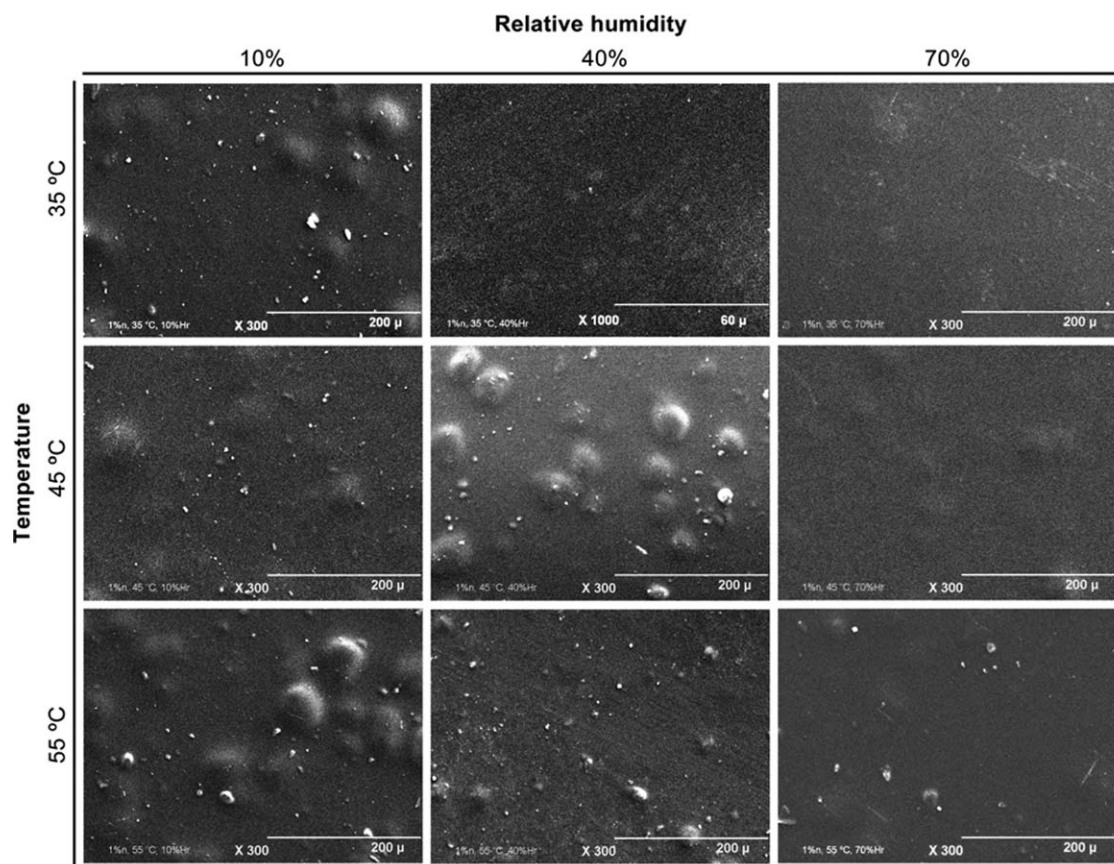
Figure 1. (a) CTA-AC Membrane micrographs obtained at different temperature, relative humidity and 1% w/v AC loading.

be obtained. Also, carbon particles are better dispersed and aggregates are not longer detected (see 35°C and 70% RH, 1% CL).

The second parameter, temperature, influences the evaporation velocity. Thus, for high temperature, the evaporation rate increases and larger carbon aggregates are formed.

The evaporation-precipitation phenomenon is also affected by carbon loading. It gives rise to additional surface tortuosity,

which plays an important role in solvent and non-solvent molecular diffusion.

In a previously reported work creep analysis was performed for all composite CTA-AC membranes presented in this study.[5] It was found that films prepared with 1% carbon loading, particularly at RH = 70% and $T = 35$°C, presented the greater dimensional stability. This fact was due to their low compliance, J, which implies the minimum strain variation in time. In this study, the same casting conditions originated the more

Table I. Number, Mean Diameter (μm), and Standard Deviation of the Aggregates for CTA-AC Membranes Obtained at 1% Carbon Loading

	Number			Size (microns)		
	Relative humidity			Relative humidity		
Temperature	10%	40%	70%	10%	40%	70%
			Load: 1%			
35°C	14	10	0	37.4 (4.9)	5.2 (0.4)	No detection
45°C	14	17	17	39.6 (3.9)	35.0 (5.1)	33.4 (2.8)
55°C	20	0	7	36.3 (5.8)	No detection	42.4 (8.0)
			Load: 3%			
35°C	0	0	0	No detection	No detection	No detection
45°C	19	42	36	36.6 (3.7)	24.8 (2.4)	27.0 (2.8)
55°C	0	50	23	No detection	16.7 (1.9)	31.1 (4.4)
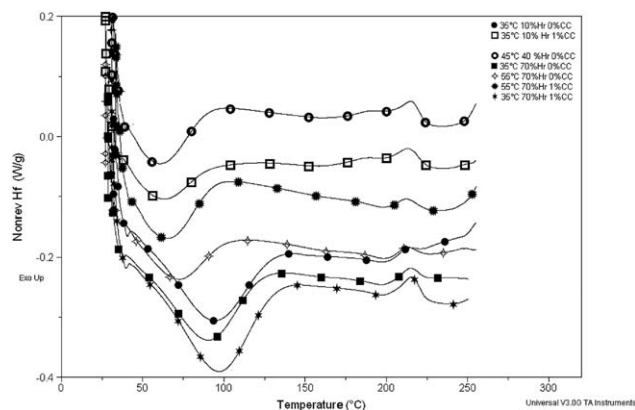
Figure 2. MDSC from 28 to 265°C, 5°C min^{-1} and modulated 1°C/80 s, in air. Nonreversible flux (Nonrev Hf) vs. temperature.

homogeneous films. This means that composite homogeneity guarantees a better mechanical performance of the films. For instance, the further analysis was done with composites obtained just with 1% AC loading, in order to elucidate their structural changes due to the temperature and relative humidity adjusted during the precipitation of the film.

Dynamic Mechanical Analysis (DMA) and MSDC

With the aim to understand the interaction of the diverse components in the internal structure of the homogeneous membranes obtained (at 1% CL), a modulated scanning calorimetry was performed (MDSC). It has been demonstrated to be a very powerful tool to understand the influence of fillers within polymeric matrixes during the thermal transitions.[30–35] Using MDSC, the reversible and nonreversible heat flow curves could be separated independently and therefore, the different temperature effects on the molecular structure could be pointed out.

For all the membranes evaluated, the reversible heat flow curves showed no variation within temperature and humidity. Meanwhile, as it is shown in Figure 2, there were different irreversible signals for CTA composite membranes. Samples prepared at the higher RH (70%) and lower temperature (35°C) presented the major endothermic transition (around 100°C). This revealed the presence of water trapped into the film internal structure. Thus, it can be postulated that water is acting as a plasticizer,[15] integrating filler into the polymer, promoting a better dispersion. This condition is only attained when low temperature is used. As can be observed in Figure 2, the same RH condition for 55°C is not evidencing the same water transition, neither for 45°C. So, water diffusion into the polymeric matrix is more effective when low temperature is used during casting, a fact that has given rise to better structural composite characteristics.

In a CTA organic solution, anisotropic aggregates are formed.[36] Upon the transition from the polymer solution to a film, different domains are evolved, i.e., regions with a local orientation order obtained due to the aggregation of macromolecules segments. Unlike cellulose, CTA is unable to form intermolecular hydrogen bonds. Because of this, solid CTA presented mainly amorphous regions with a minimum crystalline domain. This explains the other transition evidenced in the nonreversible heat flow curves; the minimum crystallization peak is around 230°C.

With the intention of elucidating the water effect during the synthesis in the composite structure, a DMA test was carried out for the membranes obtained at 70% RH.

DMA has been widely used for the viscoelastic analysis of polymers and the study of the interacting components in polymeric composites.[37–40] The analysis is in correlation to the material stiffness. Several graphs of tan of delta angle (tan δ) were obtained from the dynamic tests, and the glass transition temperatures (T_g) calculated from them are presented in Table II. The glass transition temperature is defined as the maximum in the transition curve of the loss modulus, or the maximum in the loss curve of tan δ. The results stated in Table II correspond to the second definition. Similarly, from the stain–stress curves, the Young modules are obtained. The E' value at 100°C is a measurement of the elastic behavior of a membrane when bulk water, which is not held in the hydrophilic binder polymer layer, has been evaporated. From data in Table II the following statements are evolved:

1. The moduli values E', at 100°C show the same tendencies than the Young moduli obtained at low casting temperature. Activated carbon strengths the composite, producing more resistant and less fragile membranes. Even if the temperature is fixed at 100°C for the analysis, and trapped water is no longer present, the moduli are greater for the more homogeneous composites. This suggests that water evidenced by MSDC is actually forming a solvation sphere in the matrix structure, and is not only trapped by the pores. A higher casting temperature is not allowing water molecules to penetrate the composite, and carbon is no longer reinforcing enough the material, in such cases.

2. T_g is reduced when carbon is included in the polymer at low casting temperature. CTA is a semicrystalline polymer[41]; for instance, T_g should depend upon: the crystalline domain, the free volume of the amorphous region and the interaction among both of them. In the case of composites, carbon is also contributing to T_g of the polymer; it could create additional free volume within the membrane. Considering that the water is trapped into the composite formed when low casting temperature is used, it is confirmed that in the presence of AC, water is acting as plasticizer, lowering T_g. This effect is no longer evidenced at the highest casting temperature (55°C).

Table II. Mechanical Properties for Membranes Obtained at 70% RH

Sample	Young moduli (Gpa)	E' 100°C (Mpa)	T_g (°C)
350	1.10	1.355	194 ± 1.1
351	1.30	1.514	187 ± 1.2
450	1.05	1.196	188 ± 0.9
451	1.00	1.178	187 ± 0.8
550	0.90	495	174 ± 0.55
551	0.75	669	192 ± 0.88

Samples identification is as follows, the first two numbers correspond to temperature, and the third corresponds to %AC loading; id, 351:35°C and 1% AC.
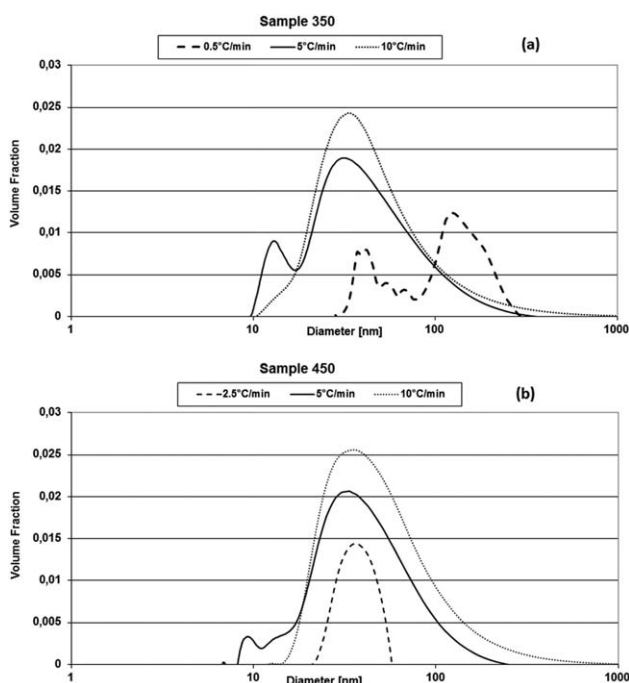
Figure 3. Pore size distribution for samples 350 (a) and 450 (b) calculated from DSC measurements at different cooling-heating rates.

Thus, it seems interesting to evidence the slight differences among composites synthesized at 35 and 45°C. Both of them present high moduli (Young moduli and E') but, at 45°C, there is neither homogeneity (regarded as the number of aggregates, Table I), nor a clear contribution in T_g. Thus, it was decided to analyze their structural changes further, and obtain their pore size distributions by calorimetric and microscopic techniques.[42,43]

Membrane Characterization by Thermoporometry

In thermoporometry, a differential scanning calorimeter is properly suited for precise measurement of the relatively small temperature shifts, because of its particular sensitivity to exothermic freezing and endothermic melting transitions. The physical basis for this is that the equilibrium temperature for a solid–liquid phase transition is determined by the radius of curvature of the interface between the solid and the liquid phases. A liquid held inside a porous material is finely divided; therefore, the radius of curvature is closely related to the pore size.

In the scientific literature, there is not a universal protocol for DSC temperature programs, as experimental conditions are often directed by many variables: the characteristics of the porous solid, the solidification temperature of pore-filling liquid, the sample size and the instrument capabilities.[44] Thus, membranes were previously characterized by DSC using different, heating-cooling rates. In previous studies with cellulose derivatives materials, it has been observed that the relative amount of bulk and pore water indicated by the heat-flow versus temperature plots depends on the heating rate used in the DSC experiment. This was ascribed to the refreezing of water melted below 0°C, given sufficient time, and its subsequent remelting along with bulk water. If bulk water existed outside

the cellulose, re-freezing would appear to involve migration of water from within the cellulose during the DSC experiment to the surface.[15,45]

Membrane prepared without carbon loading identified as 350 and 450 (35 and 45°C, respectively; 70% RH) were characterized at three different heating-cooling rates, in the interval of 0.5–10°C min^{-1}. Figure 3 shows the pore distribution calculated from the thermograms obtained at different heating-cooling rates for these samples. As expected, the shape of the curve changes from one rate to other quite dramatically.

For the cooling rate of 10°C min^{-1}, the shapes of the pore size distribution always shifted to bigger pore sizes. So that, the total pore volume appeared to be five to eight times larger than those calculated with the results from other rates. In the heating part of the experiment, the temperature in the program was set to −0.15°C. With a heating rate as fast as 10°C min^{-1} the equipment was not able to stop at exactly −0.15°C, but went on up to 2.5°C. Therefore some of the bulk water on the sample was also melted, and it is seen on the crystallization part of the thermogram, confounded as bigger pores. Also, a fast rate (10°C min^{-1}) did not permit to see the smallest pores of the distribution, since they got covered in the huge heat-flow curve.

At extremely slower rates (0.5°C min^{-1}), the time in which the sample was held at temperatures so close to 0°C, also permitted some of the bulk water to melt, and most of the times refreezed. Therefore, results at these rates gave extremely high volumes and were hardly reproducible. The different cooling–heating rates tested, were adjusted in order to enable the resolution needed for the porosity present in the material. To transform a DSC profile into a size distribution, the temperature data is transformed into an equivalent length scale (pore radius) and the heat flow output from the melting or solidification into a differential pore volume. Low scan rates are usually adjusted for narrow size distributions, taking into account that the total pore volume calculated should never overpass the water adsorption isotherms previously recorded; otherwise by this technique, water from the bulk could be confounded as bigger pores. For the cooling rate of 10°C min^{-1} the total pore volume appear to be five to eight times larger than those calculated with the results from 5°C min^{-1}, because in those conditions some of the bulk water on the sample was also melted and it is seen on the crystallization part of the thermogram. This is an erroneous calculation so that it was the criteria to select the indicated rate.

For this reason, in this study we do not consider the total pore volume obtained from the data of the thermograms, but we affirm that the pore size distribution determined at the rate of 5°C min^{-1} can be considered correct, since the total volume obtained in those experiments never overpassed the values obtained with the water vapor adsorption isotherms.[7]

The cumulative pore size distributions for samples 350 and 450 are shown in Figure 4. From these curves we calculated the mean pore size from the value at 50% of the total volume. These kinds of graphs were obtained for the following techniques used for pore size measurement. The shape for all of them is clearly the same, as it is an accumulation of the pore size distribution data. Results are shown on Table III. It can be seen
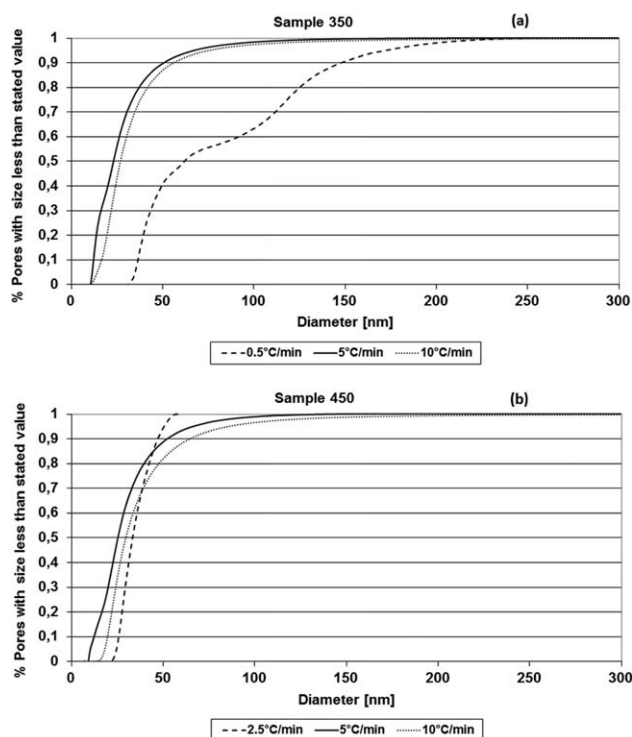
Figure 4. Cumulative pore size distributions for samples 350 (a) and 450 (b) calculated from DSC measurements at different cooling-heating rates.

that the mean pores size remains around the same value, with an experimental error, for cooling rates above 2.5°C min^{-1}.

Considering these results, further thermoporometry measurements were made at a heating–cooling rate of 5°C min^{-1}. For each sample, two replicates were made with two consecutives runs of the DSC program. In total, 24 experiments were made. The results are the average of six experiments for each membrane preparation condition. The consecutives runs did not change the pore size distribution and the pore volume, so no damage was made into the membrane structure by the crystal formation of water inside the pores. Figure 5 shows the pore size distribution for membranes prepared at the four different conditions. These are selected based on the results obtained in the previous experiments. In all of the preparation conditions we observed a small fraction of pores that have a diameter below 12 nm (see the undulation in Figure 5), and the main pore volume which is around 25 nm of diameter (maximum in the distribution). Water $\Delta H_f = 333$ J g^{-1} is up to an order of magnitude larger than most organic liquids. This magnitude

Table III. Mean Pore Size of Samples 350 and 450 Obtained by Thermoporometry at Different Cooling Rates

| Sample | Cooling rate (°C min^{-1}) | | | |
	0.5	2.5	5	10
350	61.81	–	22.95	26.6
450		33.02	25.09	28.94

Diameters are given in (nm).
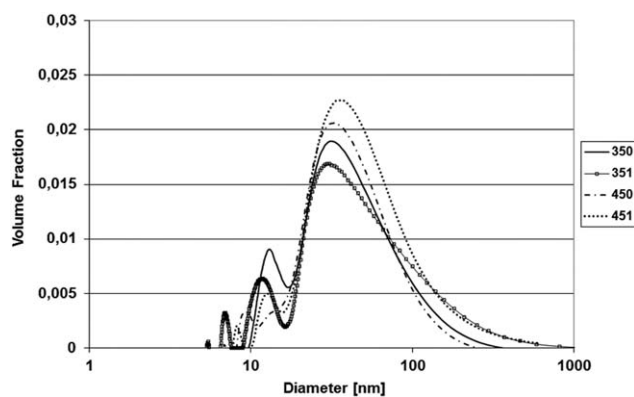
Figure 5. Pore size distribution for samples 350, 351, 450, and 451 calculated from DSC measurements, cooling at 5°C min^{-1}.

enhances the sensitivity of DSC to small volumes of adsorbed liquid[44] [refer to eq. (2)], allowing to discern the fine pore distribution at the smaller pore size values. Both temperature of preparation and carbon loading affect curve shape. The carbon loading increased the fraction of pores with bigger size. Theoretically temperature and the pore size are related by the Gibbs–Thompson equation. The pore size is proportional to the temperature depression rather than the absolute temperature; therefore, the onset temperature for the bulk phase melt must be subtracted from the temperature axis of the DSC profile. The result is a rescaled temperature axis T that can be directly transformed into pore radius r_P. This algorithm could provide some bias to the final calculation of the mean pore size. Nevertheless, Figure 5 shows how volume fraction is increased from the nonloaded membranes to the ones that are AC filled, i.e., Total pore volume is greater for the composites where AC is added.

The cumulative pore size distributions were acquired from pore size distributions. From these curves we calculated the mean pore size from the value at 50% of the total volume, and the molecular weight cut off (MWCO) at 90%, which are shown on Table IV. The mean pore sizes and the MWCO were smaller for the membranes prepared at 35°C, but at both temperatures of preparation the carbon loading shifted these sizes to higher values.

To consider a membrane casting system as vapor-induced phase separation (VIPS), the mass transfer path of the polymer has to reach the bimodal curve of the ternary system, before all the solvent has been evaporated from the solution. In the modeling and simulation of non solvent vapor-induced phase separation, it was found that for a high miscibility system, such as the one conformed by cellulose-acetone-water, the minimum relative humidity to induce phase separation was 68%.[29] During our experiments, 70% RH was maintained at all times during the casting of the membranes, so a cellulose triacetate/dichloromethane/water ternary system was conformed.

During the VIPS process, there is water inflow from the humid atmosphere to the film and outflow of volatile methylene chloride by evaporation from the film to the air phase. The water flux at the interface is negative, which means there is absorption of water, up to a few seconds before the precipitation point;

Table IV. Mean Pore Size (µ), Molecular Weight cut off (MWCO), Standard Deviation (σ) and Pore Density (N) of Samples 350, 351, 450, and 451 Obtained by Thermoporometry, Solute Transport and AFM

Sample	Thermoporometry		Solute transport				AFM		
	µ (nm)	MWCO (kDa)	µ (nm)	σ (nm)	MWCO (kDa)	N (pores µm^{-2})	µ (nm)	σ (nm)	MWCO (kDa)
350	22.95	571	30.99	1.69	801.15	6.055	9.50	2.12	175.10
351	23.02	654	35.34	1.84	1,194.29	7.329	11.59	2.67	404.76
450	25.02	611	35.56	1.65	950.06	19.152	10.56	2.02	187.55
451	26.60	721	54.91	1.94	2,860.57	2.461	19.38	2.13	594.91

meanwhile the methylene chloride flux at the interface is always positive. The water flux into the film starts at a high value, and then decreases to a plateau, finally reversing itself at the point where the water and methylene chloride fluxes become equal. There is eventually no driving force for water diffusing into the film because of its minimal concentration gradient across the film–air interface; after that, it begins to evaporate from the system. This mass transfer path will result in the formation of pores in the membrane structure.

Decreasing the air temperature leads to slower evaporation of methylene chloride from the solution-air interface and decreased water concentration inside the film, leading to a more dense structure of the membranes.

When carbon is added into the polymeric matrix, some effects could affect directly the porosity:

1. Carbon tortuosity and the molecule path for the diffusion of both, solvent and nonsolvent, is greater and then, the casting process is slower, producing more packed materials.
2. Water affinity is greater when carbon distributes finely into the polymer, and its own porosity could increment the total porosity in membrane.
3. The composite is more hydrophilic, producing some hydrogen bonding with water and carbon particularly. This interaction may hinder the ones established among AC and CTA, leading to a less dense structure in the composite. In other words, the water hydrogen bonded to carbon acts as the transient template for the increase in free volume of the forming composite.

The final effect is the porosity increment in composites, remarked at 45°C by this technique.

**Membrane Characterization by Solute Transport**
Figure 6 shows the log-normal probability plot of PEG-PEO separation data versus solute diameter, using membranes prepared at 35 and 45°C, 70% RH. The linear correlations present high coefficients, (>0.9), indicating that this function is appropriate to describe pore size distribution in CTA-AC composite membranes. Probability density curves are in Figure 7. Mean pore size (µ), molecular weight cut off (MWCO), pore density (N) and standard deviation (σ) (Table IV), were calculated from solute transport experiments.[24] By this technique differences among 35 and 45°C casting temperatures are more evident. The results show the expected trend at lower temperature: smaller pore size in the membranes is evidenced. Other

authors have reported that the mean pore size and MWCO by solute transport were decreased by increasing the solvent evaporation time in PES membranes obtained by evaporation-precipitation.[46]

Carbon loading has also an impact on pore size distribution. AC particles had a tendency to agglomerate, promoting macropores formation. This accounts for the increment in mean pore size of the composites. It is notorious the difference in their particular morphological features (Table IV). Thus, porosity is greater when agglomeration of AC is attained in the case of using 45°C. These findings are similar to the ones reported with Al_2O_3/PES nanocomposites.[47] They concluded that the MWCO data are affected by many parameters such as interrelated effects of solvent, solute, membrane properties and process conditions.
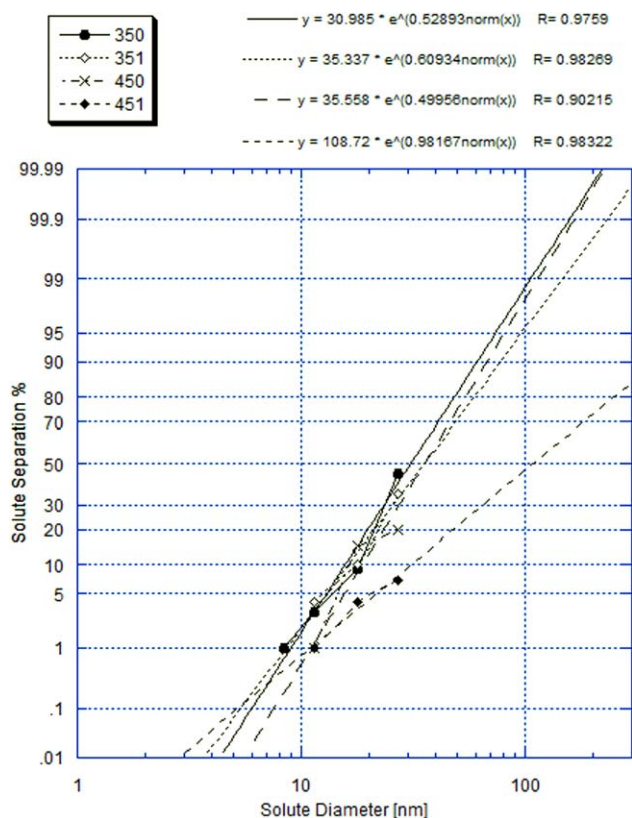
Figure 6. Solute separation curves (solute diameter versus solute separation) plotted on a log-normal scale for samples 350, 351, 450, and 451. [Color figure can be viewed in the online issue, which is available at wileyonlinelibrary.com.]
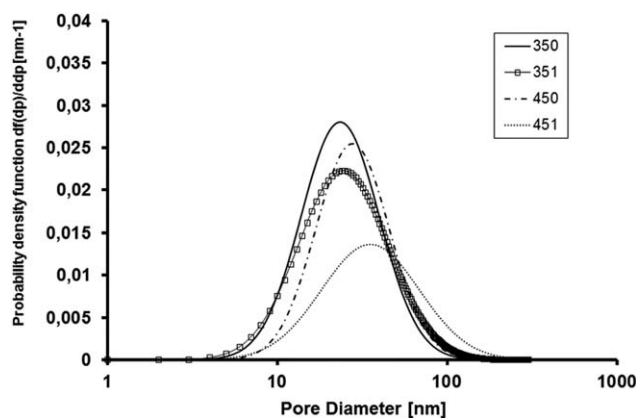
Figure 7. Probability density function curve for samples 350, 351, 450, and 451 calculated from solute transport experiments.

Also they found that the aggregation of alumina particles was greater as concentration increased and solvent rate diminished.

Atomic Force Microscopy

The four different independent samples: 350, 351, 450, and 451 membranes were analyzed by AFM. The pictures were processed using Nanoscope 5.30r3sr3® software, using the inverted image. Figure 8 shows a 3D-image of the 450 membrane and its inverted image.

For the pore analysis a special tool was used to measure the granule using the threshold parameter and considering the security interval between -1.060 and -1.087 nm as the minimum value. The program selected the images and provided the area data of each granule.

The data compiled are converted into diameter and the mean interval is calculated. Diameter versus medium intervals is shown in a log-normal plot in Figure 9.

From the linear region of Figure 9, distribution curves of the pore distribution probability function (Figure 10) were obtained.

Data on pore mean size, standard deviation and MWCO were obtained from Figure 10. Results are shown in Table IV. As it
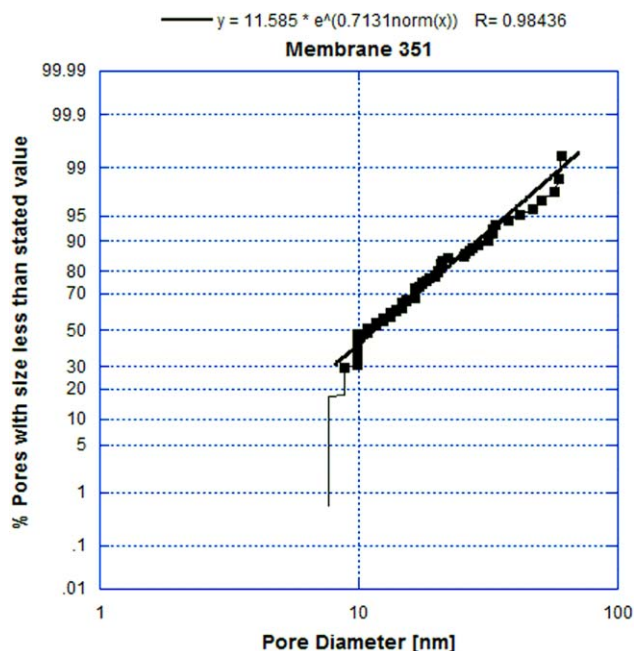

Figure 9. Log-normal distribution of the pore size by AFM. Data for membrane 350. [Color figure can be viewed in the online issue, which is available at wileyonlinelibrary.com.]

can be regarded, mean pore diameters obtained by AFM are almost a 50% lower than the ones obtained from thermoporometry and solute transport.

Previous reports on AFM analysis for pore diameter describe that, generally, higher pore size are obtained, in contrast to techniques as solute transport.[22,24] AFM data obtained are in the proximity to the real dried pore size; meanwhile, in active techniques like solute transport, the parameter obtained is the hydrodynamic pore size.[48,49] Our results evidence an increment in mean pore size for composites, in agreement with the results by the rest of the techniques evaluated. They also are in accordance with the findings in other CTA membranes,[50] where the surface porosity determined by AFM was much lesser than the internal porosity using weight analysis.
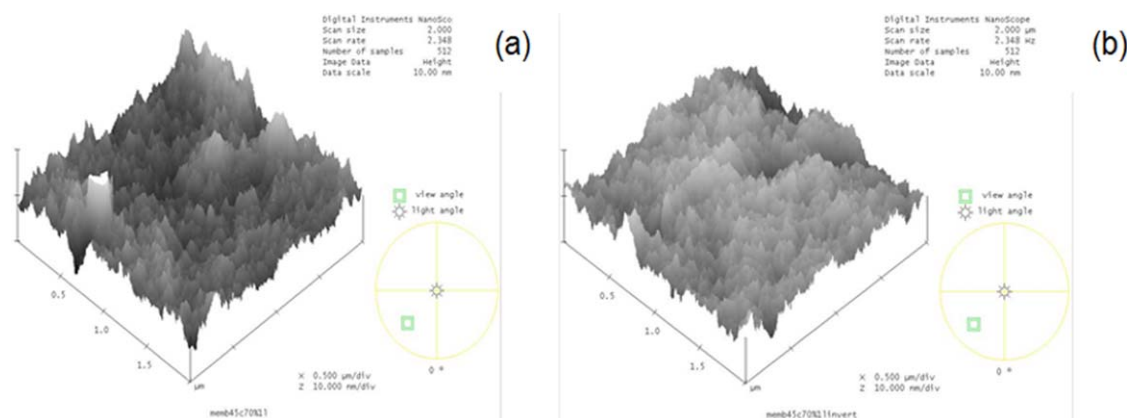
Figure 8. AFM image ($2 \ \mu m^2$) of a CTA membrane prepared at 45°C and 70% relative humidity; $z = 10$. (a) Direct image, (b) Inverted image. [Color figure can be viewed in the online issue, which is available at wileyonlinelibrary.com.]
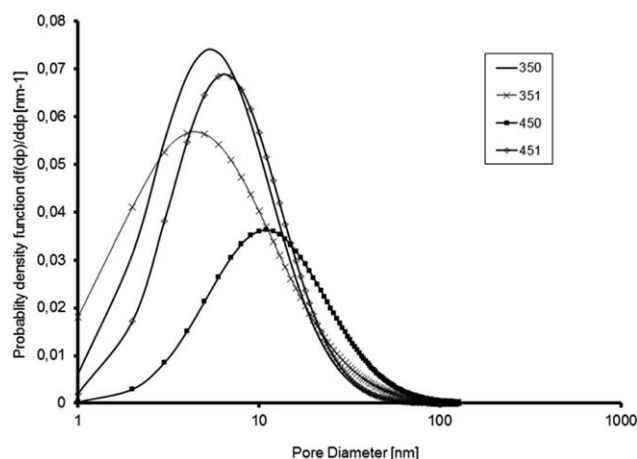
Figure 10. Probability function of the pore size density obtained from AFM images.

Arsenic Removal

The water flux was measured using the membranes synthesized at 35 and 45°C, 70% RH. This was in the interval from 1.02 to 5.23 L m^{-2} h^{-1} bar^{-1}, which corresponds in most of the cases, to a nanofiltration process.[51,52] In nanofiltration, the mechanism of rejection is more complex than a screen filtration.[51] Arsenic cannot be removed mainly by size exclusion. Other studies demonstrate that some membranes can remove arsenic compounds up to two orders of magnitude than the membrane pore size.[53] For charged solutes two additional mechanisms should be considered:

1. Donnan exclusion, promoted by the slightly charged nature of the membrane and the charged solutes. Ions with different charge (counter-ions) are attracted, while solutes with a similar charge (co-ions) are repelled. At the membrane surface a distribution of co- and counter-ions will occur, thereby causing differential rejection.
2. Dielectric exclusion promoted by the polarization of water molecules inside the pore. This polarization results in a decrease of the water dielectric constant, thereby making it less favorable for a charged solute to go into. This also results in exclusion.

As it has been previously described, water is incorporated as plasticizer and it is trapped preferably when low casting temperature is used. Water incorporation also must contribute to hydrogen bonding which facilitate water flow through the membrane structure. Besides, carbon should provide an adsorption character to membrane and probably modify the net charge of the interface exposed to the liquid phases. Its pHzc measured of 5.5, suggest that AC could be negative in charge at pH = 6.0. Nevertheless future work should be addressed to confirm this hypothesis. In nanofiltration, Donnan exclusion is strongly affected by the ionic nature of both, the membrane and feed solution. As it was mentioned, redox and pH conditions control the speciation of arsenic and for instance its ionic state. In the synthetic conditions tested, arsenic exists as As (V). No arsenite was detected neither in the permeate nor the retentate. Arsenate at pH = 6 is present mainly as the anionic compounds,

$H_2AsO_4^-$ and $HAsO_4^{2-}$ and redox potential measured was 500 mV. In Table V the results on arsenic removal with composites of CTA-AC are shown. Membranes without AC (350 and 450) rejected arsenic into concentrate flux. For the membrane with lower mean pore diameter (350), it is more evident that NF is attained. The NF process is sensitive to the ionic strength of the solution since the membrane surface charge is actually due to ion adsorption from water, rather than to fixed charged groups. Thus, for higher concentration, ion rejection is increased, a typical behavior in NF.[51] In the case of the experiments using 351 and 451 membranes, there is arsenic depletion in both, retentate and permeate solutions. The material balance of arsenic on filtrate processes suggested that removal mechanism involved also adsorption of solute into activated carbon particles inside the membranes. As it was described, in previous works AC has an important role on metal adsorption as it was included into the polymeric membrane. For uranium it was realized that AC is more effective into the membrane than during batch adsorption essays. Previous tests done with the AC in batch configuration showed that adsorption is negligible when 500 ppb of arsenic are used at pH = 6. 7 Nevertheless if the calculus of arsenic adsorbed into the membrane is done, the carbon adsorption capacity is $Q = 4$ mg g^{-1}, which is a value into the range of other reported studies on arsenic.[54] In our materials, activated carbon is increasing size pore distribution, it is promoting water to be adsorbed to conform a solvation sphere with CTA, rendering high hydrophilic character and in this process is giving an additional adsorption behavior to the membrane. Additionally an elemental analysis to activated carbon was made, and results were the following: C 87.34, Fe 0.81, O 8.6, Al 0.8, Si 2.1, and S 0.36%.[7] For instance, it could be a reasonable statement to have a fraction of arsenic forming Fe-(oxy) hydroxide precipitates or ternary metal bridging complexes in the colloid size range formed just in the cellulose acetate-activated carbon/solution interface.[55] As colloid, arsenic could also be rejected by size exclusion.

Table V. Percentage Arsenic Removal on Permeate Flux (*P*), Concentrate Flux (*C*), and Total

Sample	Feed solution (ppb)	% Arsenic removal		
		P	C	Total
350	100	21	0	21 ± 1.5
	300	31	0	31 ± 1.2
	500	33	0	35 ± 1.7
351	100	22	8	30 ± 1.1
	300	28	11	39 ± 1.9
	500	23	21	44 ± 1.8
450	100	20	0	20 ± 1.3
	300	12.5	0	12.5 ± 1.2
	500	7	2	9 ± 0.8
451	100	23	5	28 ± 1.1
	300	14	2	16 ± 1.2
	500	10	3	13 ± 1.3

Redox effects on As adsorption into carbonaceous materials, have been described by Wang and Mulligan (2006).[56] So far Arsenic reduction is not reported by cellulose, there are studies on reduction mechanism for Cr (VI) to Cr (III).[57] In this study, FT-IR spectra indicate that the reactive sites for Cr (VI) reduction were the hydroxyl groups in cellulose, which after oxidation, were transformed in carboxyl groups. The resultant Cr(III) was either bound to cellulose or released into solution. Extended X-ray absorption fine structure (EXAFS) reveal that Cr(III) was bound to cellulose by forming bidentate–mononuclear complexes with carboxyl groups, which resulted from the oxidation of hydroxyl groups. In our study trivalent arsenic was analyzed in both retentate and permeate solutions. No reduction of arsenic was attained outside the membrane material. But is still a probability to have a reduction in the interface as it is explained below.

Commercial cellulose triacetate is not totally acetylated. The hydroxyl fraction that remains could present a similar behavior than the one reported for the chromium system. Nevertheless, the latter is a strong oxidant redox pair ($E_o = 1.33$ V), compared to the Arsenic system potential ($E_o = 0.33$ V). In a redox reaction, the electron donor and acceptor must first form an inner or outer-sphere complex, and then electron transfer occurs between the redox couple. If oxidation could occurs, arsenic must be first bound to cellulose before it can be reduced to As (III). The determination of the oxidation state and bonding geometry of As bound to cellulose after the reduction could be corroborated using X-ray absorption near edge structure (XANES) and (EXAFS).

Other important observation is the arsenic rejection improvement, according to its concentration when using membrane 351. Different studies concerning the removal of As from water by NF, where arsenic rejection increases with its retentate concentration, were reported by other authors as well.[58–61] For experiments performed with 450 and 451 membranes, such behavior is not attained. While flux characteristics and operational transmembrane pressure is in accordance with a NF process, it is reaching the limit of a reverse-osmosis process. So that, for higher concentration, lower rejection is achieved. This also could be explained considering the macro porous structure of the membranes. MWCO for the composites obtained at high casting temperature were the largest. Although in the present experiments, total arsenic removal reached only 45% under the best conditions, the results suggest that modifying preparation conditions, as well as incorporating a mechanism to fully disperse carbon particles into polymer matrix, could reduce pore size formation and increase arsenic removal.

CONCLUSIONS

The present work is an exhaustive study on composite membranes formed with Cellulose triacetate and Activated carbon. They were obtained by an evaporation-precipitation method, controlling temperature and relative humidity during synthesis. The physicochemical properties of the membranes were affected by these parameters; because they determine the evaporation rate of the solvent (CH_2Cl_2) and the diffusion of the non

solvent (water) during the film precipitation. When AC is added in most of the conditions proved, particle aggregates are formed in the composite. This behavior is diminished if the solvent diffusion is slow, attained at a low casting temperature; and in the presence of high water concentration during VIPS process.

MSDC reveals the presence of water molecules trapped into the structure for all the films obtained at 35°C by the endothermic transition around 100°C. The major transition was evidenced at 70% RH. Water is also acting as plasticizer in the composite. When AC is used in such conditions, the rate penetration of the non solvent is increased in the nascent material, due principally to its high hindrance. Thus, T_g is lower for 351 composite (187°C), contrasting with the transition observed with the membrane 350 (194°C).

Mechanically, AC addition produced the most resistant and less fragile membranes. The highest Young module (1.3 GPa) was determined for the composite 351 where the best particle dispersion was attained.

For all the techniques tested for porosity measurement, the same tendencies are evidenced. They reveal that carbon loading increased the fraction of pores with bigger size, increasing thus MWCO for the analyzed membranes. Solute transport experiments gave around 15% higher mean pore size values than the ones measured by thermoporometry. The last does not account for the water that the binder polymer may absorb and prevent from freezing. AFM was useful for porosity determination in the dried membrane conformation.

The removal of arsenic was more efficient with these composites when better particle dispersion is achieved and at high arsenic concentration. This process corresponds to a hybrid membrane one, where AC and the polymer play a transcendental role for rejection. Thus, the best conditions found for CTA- 1% AC composite synthesis, from a morphological, mechanical and hydrodynamic point of view, were obtained using a casting temperature of 35°C and 70% RH.

REFERENCES

1. Brandhuber, P.; Amy, G. *Desalination* **2001**, *1140*, 1.

2. Comisión Nacional del Agua Estudio Hidrológico, Hidrogeoquímico y de la Incidencia de Arsénico, Flúor y Hierro en las Zonas Acuíferas de Delicias-Meoqui y Jiménez-Camargo, Chihuahua Gerencia de Aguas Subterráneas: México, **1996**; (Laboratory report).

3. Manjarrez, L. A.; Ballinas, M. L.; Celzard, A.; Fierro, V.; Solís-Canto, O.; Ibarra-Gómez, R.; González-Sánchez, G. *Carbohydr Polym.* **2011**, *86*, 732.

4. Manjarrez-Nevárez, L. A.; Ballinas, L.; Celzard, A.; Fierro, V.; Torres-Muñoz, V.; Camacho-Davila, A.; Torres-Lubian, J. R.; González-Sánchez, G. *Sci. Technol. Adv. Mater.* **2011**, *12*, 045006 1–16.

5. Ballinas-Casarrubias, L.; Terrazas-Bandala, L. P.; Ibarra-Gómez, R.; Mendoza-Duarte, M. E.; Manjarrez-Nevárez, L; González-Sánchez, G. *Polym. Adv. Tech.* **2006**, *17*, 1.

6. Coelho-Nakanashi, S.; Gonçalves, A. R.; Rocha, G.; Ballinas, L.; Gonzalez, G. *Desalination Water Treat.* **2011**, *27*, 66.

7. Terrazas-Bandala, L. P.; Ballinas-Casarrubias, L.; Pardo-Rueda, J.; Manjarrez-Nevárez, L.; González-Sánchez, G. *Water 3rd IWA Young Researchers Conference*, **2006**, Nanyang Technological University, Singapore.

8. Ballinas, L.; Torras, C.; Fierro, V.; Garcia-Valls, R. *J. Phys. Chem. Solids* **2004**, *65*, 633.

9. Villalobos-Rodríguez, R.; Montero-Cabrera M. E.; Esparza-Ponce, H.; Herrera-Peraza, E.; Ballinas-Casarrubias, L. *Appl. Radiat. Isotopes* **2012**, *70*, 872.

10. Anson, M.; Marchese, J.; Garis, E.; Ochoa, N.; Pagliero, C. *J. Membr. Sci.* **2004**, *243* 19.

11. García, M.; Barsema, J.; Galindo, R. E.; Cangialosi, D.; Garcia-Turiel, J.; Van Zyl, W. E.; Verweij, H.; Blank, D. H. A. *Polym. Eng. Sci.* **2004**, *44*, 1240.

12. Torras, C.; Ferrando, F.; Paltakari, J.; Garcia-Valls, R. *J. Membr. Sci.* **2006**, *282*, 149.

13. Nakao, S. I. *J. Membr. Sci.* **1994**, *96*, 131.

14. Brum, M.; Lallemand, A.; Quinson, J. F.; Eyraud, C. *Thermochim. Acta.* **1977**, *21*, 59.

15. Hay, J. N.; Laity, P. R. *Polymer* **2000**, *41*, 6171.

16. Zhao, C.; Zhou X.; Yue, Y. *Desalination* **2000**, *129*, 107.

17. Beurroies, I.; Denoyel, R.; Llewellyn, P.; Rouquerol, J. A. *Thermochim. Acta* **2004**, *421*, 11.

18. Salles, F.; Beurroies, I.; Bildstein, O.; Jullien, M.; Raynal, J.; Denoyel, R.; Van-Damme , H. *Appl. Clay Sci.* **2008**, *39*, 186.

19. Zeman, L.; Tkacik, G. *J. Membr. Sci.* **1987**, *32*, 329.

20. Cuperus, F. P.; Bargeman, D.; Smolders, C. A. *J. Membr. Sci.* **1992**, *66*, 45.

21. Ishikiriyama, K.; Sakamotoa, A.; Todokia, M.; Tayamab, T.; Tanakabe, K.; Kobayashib, T. *Thermochim. Acta* **1995**, *267*, 169.

22. Gumí, T.; Valiente, M.; Khulbe, K. C.; Palet, C.; Matsuura, T. *J. Membr. Sci.* **2003**, *212*, 123.

23. Khulbe, K. C.; Hamad, F.; Feng, C.; Matsuura, T.; Khayet, M. *Desalination* **2004**, *161*, 259.

24. Singh, S.; Khulbe, K. C.; Matsuura, T.; Ramamurthy, P. *J. Membr. Sci.* **1998**, *142*, 111.

25. Hsieh, F. H.; Matsuura, T.; Sourirajan, S. *Ind. Eng. Chem. Process Des. Dev.* **1979**, *18*, 414.

26. Youm, K. H.; Kim, W. S. *J. Chem. Eng. Jpn.* **1981**, *24*, 1.

27. Torras, C. *Obtenció de membranes polimeriques selectives PhD thesis.* Universitat Rovira i Virgili, Spain, **2006**.

28. Puigdomenech, I. Hydra/Medusa Chemical Equilibrium Database and Plotting Software, Inorganic Chemistry; KTH Royal Institute of Technology, Stockholm, Sweden, **2009**. Available at: https://sites.google.com/site/chemdiagr/.

29. Yip, Y.; McHugh, A. J. *J. Membr. Sci.* **2006**, *271*, 163.

30. Esteves, A. C.; Barros-Timmons, A. M.; Martins, J. A.; Zhang, W.; Cruz-Pinto, J.; Trindade, T. *Compos. B.* **2005**, *36*, 51.

31. Fang-Chyou, C.; Sun-Mou, L.; Yu-Lun, C.; Tsung-Han, L. *Polymer* **2005**, *46*, 11600.

32. Fang-Chyou, C.; Pei-Hsien, C. *J. Polym. Res.* **2006**, *13*, 73.

33. Chen, W.; Tao, X.; Xue, P.; Chenget, X. *Appl. Surface Sci.* **2005**, *252*, 1404.

34. Perrin-Sarazin, F.; Ton-That, M. T.; Bureau, M. N.; Denault, J. *Polymer* **2005**, *46*, 11624.

35. Jain, S.; Goossens, H.; Van Duin, M.; Lemstra, P. *Polymer* **2005**, *46*, 8805.

36. Novikov, D. V.; Krasovskii, A. N.; Matasakanov, S. S. *Phys. Solid State.* **2012**, *54*, 409.

37. Díez-Gutiérrez, S.; Rodríguez-Pérez, M. A.; De Saja, J. A.; Velasco, J. I. *Polymer* **1999**, *40*, 5345.

38. Arrighia, V.; McEwena, I. J.; Qiana, H.; Serrano-Prieto, M. B. *Polymer* **2003**, *44*, 6259.

39. Yasmin, A.; Luo, J. J.; Abot, J. L.; Daniel, I. M. *Compos. Sci. Tech.* **2006**, *66*, 2415.

40. Deng, J.; Xiaoqin, Z.; Ke, W.; Hao, Z.; Qin, Z.; Qiang, F. *J. Membr. Sci.* **2007**, *288*, 261.

41. Mandelkern, L.; Flory, P. J. *J. Am. Chem. Soc.* **1951**, *73*, 3206.

42. Causserand, C.; Aimar, P. In Comprehensive Membrane Science and Engineering: Basic Aspects of Membrane Science and Engineering; Drioli, E., Giorno, L., Eds.; NorthHolland/American Elsevier: Amsterdam, **2010**; Vol. *1*, p 311.

43. Fane, A. G.; Tang, C. Y.; Wang, R. Treatise on Water Science: Water-Quality Engineering; Peter, W., Ed.; NorthHolland/American Elsevier: Amsterdam, **2011**; Vol. *4*, p 301.

44. Landry, M. R. *Thermochim. Acta* **2005**, *433*, 27.

45. Higuchi, A.; Komiyama, J.; Iijima, T. *Polym. Bull.* **1984**, *11*, 203.

46. Mosqueda-Jiménez, D. B.; Narbaitz, R. M.; Matsuura, T.; Chowdhury, G.; Pleizer, G.; Santerre, J. P. *J. Membr. Sci.* **2004**, *231*, 209.

47. Zwijnenberg, H. J.; Dutczaka, S. M.; Boerrigtera, M. E.; Hempeniusc, M. A.; Luiten-Oliemand, M. W. J.; Benesb, N. E.; Wessling, M.; Stamatialise, D. *J. Membr. Sci.* **2012**, *390/391*, 211.

48. Kim, S.; Chen, L.; Johnson, J. K.; Marand, E. *J. Membr. Sci.* **2007**, *294*, 147.

49. Fritzsche, K.; Arevalo, A. R.; Connolly, A. F.; Moore, M. D.; Elings, V.; Wu, C. M. *J. Appl. Polym. Sci.* **1992**, *45*, 1945.

50. Yamazaki, K. J.; Matsuda, K.; Yamamoto, K.; Yakushiji, K.; Sakai, K. *J. Membr. Sci.* **2011**, *368*, 34.

51. Mulder, M. Basic Principles of Membrane Technology; Kluwer Academic Publishers: The Netherlands, **1997**.

52. Hussain, A. A.; Nataraj, S. K.; Abashar, M. E. E.; Al-Mutaz, I. S.; Aminabhavi, T. M. *J. Membr Sci.* **2008**, *310*, 321.

53. EPA 815-R-00–028. Technologies and Costs for Removal of Arsenic from Drinking Water; **2000**; p 2.

54. Fierro, V.; Muñiz, G.; González-Sánchez, G.; Ballinas, M. L.; Celzard A. *J. Hazard. Mater.* **2009**, *168*, 430.

55. Lin, H. T.; Wang, M. C.; Li, G. C. *Chemosphere* **2004**, *56*, 1105.

56. Wang, S.; Mulligan, C. N. *Environ. Geochem. Health.* **2006**, *28*, 197.

57. Shan, L.; Wanga, J. F. L. *Chem. Eng. J.* **2011**, *174*, 289.

58. Velizarov, S.; Crespo, J. G.; Reis, M. A. *Rev. Environ. Sci. Biotech.* **2004**, *3*, 361.

59. Sato, Y.; Kang, M.; Kamei, T.; Magara, Y. *Water Res.* **2005**, *36*, 3371.

60. Saitua, A. H.; Campdero, S. M.; Cerutti, S.; Padilla, A. P. *Desalination.* **2005**, *172*, 173.

61. Figoli, A.; Cassano, A.; Criscuoli, A.; Mkozumder, M. S. I.; Uddin, M. T.; Islam, M.; Drioli, E. *Water Res.* **2010**, *44*, 97.